A GPU-based solution for ray tracing 3D radiative transfer model for optical images

Zunjian Bian, Jianbo Qi, Jean-Philippe Gastellu-Etchegorry, J. -L. Roujean, Biao Cao, Hua Li, Yongming Du, Qing Xiao, Qinhuo Liu

A GPU-based solution for ray tracing 3D radiative transfer model for optical images

Journal:	*Geoscience and Remote Sensing Letters*
Manuscript ID	GRSL-00900-2022
Manuscript Type:	Letters
Sub-topic:	Vegetation and Land Surface
Date Submitted by the Author:	26-May-2022
Complete List of Authors:	Bian, Zunjian; Chinese Academy of Sciences Aerospace Information Research Institute, State Key Laboratory of Remote Sensing Science Qi, Jianbo; Beijing Forestry University, College of Forestry Gastellu-Etchegorry, Jean-Philippe; CESBIO, CESBIO Roujean, Jean-Louis; CESBIO, CESBIO Cao, Biao; Chinese Academy of Sciences Aerospace Information Research Institute, State Key Laboratory of Remote Sensing Science Li, Hua; Chinese Academy of Sciences Aerospace Information Research Institute, State Key Laboratory of Remote Sensing Science Du, Yongming; Chinese Academy of Sciences Aerospace Information Research Institute, State Key Laboratory of Remote Sensing Science Xiao, Qing; Chinese Academy of Sciences Aerospace Information Research Institute, State Key Laboratory of Remote Sensing Science Liu, Qinhuo; Chinese Academy of Sciences Aerospace Information Research Institute, State Key Laboratory of Remote Sensing Science; University of the Chinese Academy of Sciences, College of resources and environment
Key Words:	Vegetation and Land Surface < Methodologies and Applications to

IEEE MAGNETICS LETTERS, Volume 7 (2016) Page 1 of 5 (actually, 4 pages of text maximum plus references; IEEE will place article number here)

A GPU-based solution for ray tracing 3D radiative transfer model for optical images

Zunjian Bian[1], Jianbo Qi[2], J.-P. Gastellu-Etchegorry[3], J.-L. Roujean[3], Biao Cao[1], Hua Li[1], Yongming Du[1], Qing Xiao[1], Qinhuo Liu[1]

[1] *State Key Laboratory of Remote Sensing Science, Aerospace Information Research Institute, Chinese Academy of Sciences, Beijing 100101, China*

[2] *Key Laboratory for Silviculture and Conservation of the Ministry of Education, Beijing Forestry University, Beijing 100083, China*

[3] *CESBIO - Centre d'Etudes Spatiales de la BIOsphère, CESBIO UMR 5126, 31401 Toulouse, France*

Abstract: Three-dimensional (3D) radiative transfer (RT) models are frequently recognized as a prerequisite when using high-resolution remote sensing data in heterogeneous surfaces. However, most studies of 3D RT models have been restricted to limited applications due to the low computational efficiency. Therefore, this study proposed a general processing unit (GPU)-based solution for ray tracing 3D RT model. A state-of-the-art graphics and compute application programming interface, Vulkan, was introduced to implement the RT process. A bounding box method was adopted for the computation acceleration. By comparison with a central processing unit (CPU) -based one, the performance efficiency of the proposed solution is significantly better: the simulation time of a GPU model is significantly reduced by more than 99% when facing a large-scale simulation mission. And the simulation accuracy of two solutions is similar with root mean squared errors (RMSEs) lower than 0.004, 0.017 and 0.365 K for the red, near-infrared (NIR) and brightness temperature images, respectively. An evaluation based on airborne multiangle measurements also indicated the accuracy of the proposed solution was satisfactory for simulating the red and NIR bidirectional reflectance factor and brightness temperature directional anisotropies, with RMSEs lower than 0.003, 0.019 and 0.20 K, respectively.

Index Terms— 3D model, radiative transfer, GPU, ray tracing, optical image

I. INTRODUCTION

Over the past decade, many studies have emphasized the use of high-resolution remote sensing (RS) data in agriculture and urban applications [1, 2] from satellite data sources, such as the Thermal Infrared Sensor (TIRS) onboard Landsat-series satellites [3] and the Advanced Spaceborne Thermal Emission and Reflection Radiometer (ASTER) onboard the Terra satellite [4]. Duan *et al*. reviewed these types of high-resolution thermal infrared (TIR) RS data [5]. Additionally, unmanned aerial vehicles (UAVs) offer a flexible way to capture surface RS signals at high spatiotemporal resolutions. In the context of high-resolution RS data, the 3D radiative transfer (RT) model is the most suitable tool in terms of accuracy and is capable of simulating images based on 3D objects beyond pixel limitations, and considerable progress has been made in RS 3D RT modeling studies based on flux tracing, ray tracing and radiosity theories [6-8].

After a series of upgrades, the discrete anisotropic radiative transfer (DART) model has become one of the most widely used models with applications extending from radiation budgeting to light detection and ranging (LIDAR) and fluorescence determination [9]. For simulating RS images, the large-scale RS data and image simulation framework (LESS) and a rapid radiosity method with porous individual objects (RAPID) were proposed [8, 10]. Based on a computer graphic rendering engine, LuxCoreRender, Jiang *et al*. proposed a fast 3D model for the bidirectional reflectance function (BRF) [11]. Nevertheless, difficulties remained when to simulate a large number of high-resolution RS images during a short time. Thus, the rapidity of 3D models must be further improved.

In this study, we explore a general processing unit (GPU)-based solution for fast fine-scale RT simulations for optical images. A backward ray tracing strategy, also named path tracing, is selected for simulating the RT process, and the bounding box method is introduced to organize the hierarchical structure of a 3D scene. The proposed model is evaluated based on a measured airborne dataset, and a simulated dataset generated by the central processing unit (CPU)-based 3D model (i.e., LESS) is used for intercomparison. This paper is organized as follows. In Section 2, we describe the 3D path tracing model and its GPU-based implementation. The simulated and measured datasets are presented in Section 3. The evaluation results and limitations are discussed in Section 4. Finally, Section 5 provides a short summary and expresses some perspectives.

II. METHODOLOGY

Two parts of the proposed solution are introduced: one is the theory of RT for simulating RT process, and the other is the GPU-based framework and implementation for optical images.

A. Radiative transfer theory

Compared to forward ray tracing, in which rays are generated from light sources, backward ray tracing provides an efficient way to simulate images because rays are generated from cameras, as shown in Fig. 1 (a), and the radiance can be expressed as follows:

$$L_o(q,\omega_0) = L_e(q,T,\omega_0) + \int_{4\pi} f\,(q_s,\omega_i,\omega_o,\lambda)\,L_i(q_s,\omega_i)|cos\,\theta_i|d\omega_i \quad (1)$$

where L_o represents the outgoing radiance from point q in direction ω_0, L_e represents the emission radiance from point q with temperature T, and L_i represents the incoming radiance from light sources, i.e., the sun and sky in this study, in direction ω_i. f represents the bidirectional scattering distribution function (BSDF) of

Corresponding author: F. A. Author (f.author@nist.gov). If some authors contributed equally, write here, "F. A. Author and S. B. Author contributed equally."

IEEE Magnetics Letters discourages courtesy authorship; please use the Acknowledgment section to thank your colleagues for routine contributions.
Digital Object Identifier: 10.1109/LMAG.XXXX.XXXXXXX (inserted by IEEE).

the intersected surface at wavelength λ, i.e., the bidirectional reflectance distribution function (BRDF) and bidirectional transmittance distribution function (BTDF) for reflected and transmitted rays, and θ_i represents the zenith angle between ω_i and the surface normal.

As mentioned above, when a ray intersects a facet, there are three potential contributions from reflected, transmitted, and emitted terms. The reflected (f_{diff}) and transmitted (f_{trans}) functions based on the Lambertian assumption can be expressed as follows:

$$f(q_s,\omega_i,\omega_o,\lambda)=\begin{cases} f_{diff}(q,\omega_i,\omega_o,\lambda), \omega_m\cdot\omega_o>0 \\ f_{trans}(q,\omega_i,\omega_o,\lambda), \omega_m\cdot\omega_o<0 \end{cases} \quad (2)$$

$$f_{diff}(q,\omega_i,\omega_o,\lambda)=k_L(\lambda)/\pi \quad (3)$$

$$f_{trans}(q,\omega_i,\omega_o,\lambda)=\tau_L(\lambda)/\pi \quad (4)$$

where k_L and τ_L represent the Lambertian reflection and transmittance coefficients, respectively. The division by π normalizes the diffuse light, as the incident hemisphere space that contains the BRDF or BTDF is scaled by π. ω_m represents the microsurface normal. When $\omega_m\cdot\omega_o>0$ and $\omega_m\cdot\omega_o<0$, reflected and transmitted rays occur, respectively. The BTDF is considered Lambertian over all incident and observation vectors. The emitted term was based on the Planck function. According to Kirchhoff's Law, the emissivity of a component can be calculated using 1 minus the corresponding reflectance value.

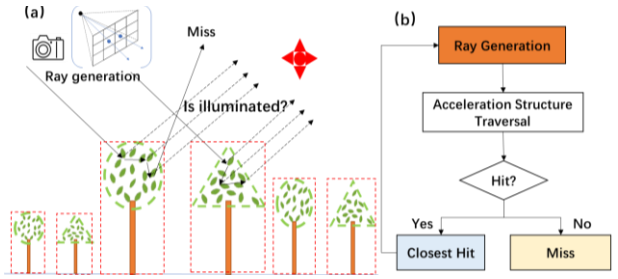

Fig. 1. (a) Schematic diagram of path tracking simulation and (b) the relationships among the three ray tracing shaders.

B. GPU-based framework

To provide improved performance and balanced central processing unit (CPU)/GPU usage, a new-generation computer and graphic application programming interface (API), Vulkan, is used in the GPU-based framework as shown in Fig. 2. This API was first released by the nonprofit Khronos Group in 2015. Detailed information on the Vulkan rendering scheme can be found at https://www.khronos.org/vulkan/. In this paper, we briefly introduce two steps used in the 3D RT model: data transfer and pipeline rendering for input/output and RT processes, respectively. All the operation instructions/descriptions for the data and the RT method must be input into the command buffer for execution.

In the Vulkan-based model, all input and output data for the renderer need to be described by the descriptor set. The input can be classified as a 3D scene structure, component material, and illuminating and viewing geometry. Background soil, vegetation canopies, and simple buildings are 3D objects currently studied, and they are all generated by using triangle facets. In the RS RT process, component materials correspond to specific optical and thermal properties, such as reflectance, transmittance, and temperature. The optical properties of leaves and soil can be obtained by PROSPECT and general spectral vector (GSV) models, respectively, and those of other components can be obtained from the ASTER library [12, 13]. In the VNIR domain, the light sources include the sun and sky, and the corresponding contributions can be determined by the direct/diffuse ratio. The viewing information depends on the position, direction, and field of view of the camera. The simulated outputs are VNIR and TIR images. When the image size is given, the pixel-based spatial resolution can be set. After rendering, the resulting images can be saved. The resulting images can also be displayed on the screen by using a structure called SwapChain, which provides an image queue.

In Vulkan, the rendering pipeline is a conceptual model that describes what steps a graphics system needs to perform to render a 3D scene to a 2D image. Obviously, the abovementioned RT theory should be bound to a rendering pipeline. In a classic graphics pipeline, a vertex shader performs basic processing steps for each individual vertex, and a fragment shader processes a fragment generated by rasterization into a set of colors and a single depth value. For the path tracing pipeline, a compute shader is used. It should be noted that to use the ray tracing method, the VK_KHR_RAY_TRACING extension should be added.

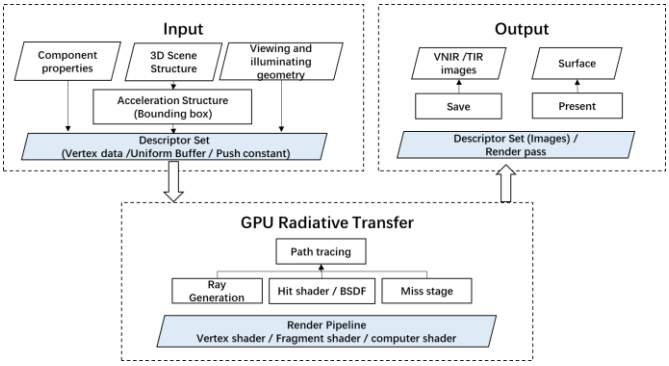

Fig. 2. The GPU-based radiative transfer framework based on the Vulkan API. The white and blue backgrounds indicate elements in radiative transfer and Vulkan implement, respectively.

C. GPU-based implementation

In the GPU-based image simulation, three shaders shown in Fig. 1(b) are used to accumulate reflected, transmitted and emitted radiance:

Ray-generation shader: A ray can be mathematically defined by a point, i.e., the origin of the ray in the space, and a direction. In primary scattering, rays are cast into a scene for each pixel in the image and are generated from the focus of the camera. It should be noted that to solve the aliasing problem, primary rays should be generated for multiple samples per pixel. After ray generation, a traversal process is implemented for each facet to determine if it is intersected by a ray. Then, two states can be identified: hit or miss. In multiscattering cases, secondary rays should be created from the previous rays at the intersection point and the direction determined by the hit shader.

Hit shader: When a facet is hit, it means that radiance leaving this facet contributes to the RS observation of a pixel. In multiscattering cases, the contribution of a hit is determined with the BSDF along the corresponding path rather than the BSDF at this hit point only. At each intersection point, an extra ray is generated in the sun direction to

determine whether it is illuminated. It should be noted that there is only one ray path for each sample, and the contribution of the hemisphere is obtained by double-importance Monte Carlo sampling [7]. In addition to the radiance contribution, the direction of the next ray is also determined in this shader.

Miss shader: If a ray does not hit any facet, a miss state exists. When rays miss the 3D scene, a default "no value" is set for primary scattering. In multiscattering cases, missing rays are considered the contribution of the sky.

To accelerate the shader traversal process, a bounding box method is adopted. As shown in Fig. 1 (a), all surface facets are organized into two levels: the bottom level includes an array of all geometries, and the top level is an imaginary rectangle referenced to a set of bottom-level structures determined for a certain instance. First, a test is performed to determine if the ray intersects the top-level box, and if it does not, we know that it cannot intersect the geometry contained in the corresponding bounding box. Otherwise, all facets contained in the box will have to be tested to determine if they are intercepted by this ray. In a large-scale scene, only a small number of adjacent facets intersect a ray. Therefore, the bounding box acceleration method can save considerable time.

III. Materials and Dataset

A. Generation of a synthetic dataset

An intercomparison with the CPU-based 3D LESS model was performed based on a synthetic dataset. A sparse forest scene was generated with an area of 100 m × 100 m, and 385 trees were randomly distributed. Individual forest canopies were simulated and were used in the LESS and the proposed models in the same way. Red and NIR reflectance and TIR brightness temperatures (BTs) were selected for comparison. Image sizes were set to 500×500 and 100×100 with spatial resolutions of 0.2 m to 1.0 m, respectively. Because the same scene structure and component properties were input, the simulated observations of the two models for each pixel were compared in addition to the VNIR BRF and BT DA values for the whole image. The comparisons of red and NIR BRF and BT DA were performed in the solar principal plane, and those of red, NIR and BT images were performed at nadir.

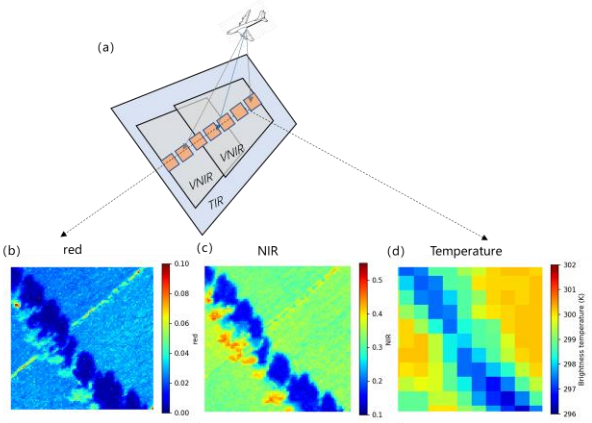

Fig. 3. (a) Schematic diagram of airborne multiangle observations of the study area; (b), (c) and (d) are images of red and NIR reflectance and TIR brightness temperatures, respectively.

B. Airborne measured dataset

The airborne measurements obtained from HiWATER (Heihe Watershed Allied Telemetry Experimental Research project) were used to test the GPU-based solution of path tracing model. The Zhangye artificial oasis is one of three key observation areas in the HiWATER study region, which is an arid region in Northwest China (Gansu Province). A large area of corn, trees near roads and scattered buildings are distributed in this region. The flight mission was performed on August 3, 2012. During the observation mission, the weather was clear and windless. Detailed information for this dataset can be found in [14].

Observations with a large viewing zenith angle (VZA) were obtained with a wide-angle infrared dual-mode line/area array scanner (WIDAS) with a TIR camera and two VNIR cameras, as shown in Fig. 3(a). In this study, a mixed scene of trees and corn was selected, with an area of 50 m × 50 m. Observations from the red, NIR and TIR bands were used with wavelength ranges of 590-670 nm, 850-1000 nm and 7.5-14.0 μm, respectively. All observations were organized and saved in a multiangle dataset after radiation calibration, atmospheric correction, and geometric correction. The study area was mainly located in the middle of the image, so the observations were obtained with VZAs ranging from approximately 0° to 50° with a step of 5° and at a viewing azimuth angle (VAA) of 120°. The Beijing time for these data was approximately 11:28; at this time, the solar zenith angle (SZA) was 34.4°, and the solar azimuth angle (SAA) was 122.8°.

During the airborne experiment, the reflectance values of the understory soil background of the crops and tree belts were measured in the field using a FieldSpec Pro spectrometer (Analytical Spectral Devices), and the hemispherical reflectance and transmittance of leaf samples from crops and tree belts were measured with an ultraviolet–visible spectrophotometer with an integrating sphere in the laboratory [15]. The emissivity of components was obtained from measurements with an ABB BOMAN spectroradiometer. Unique sunlit and shaded temperatures were assumed for each component, and these temperatures were obtained with contact thermometers. According to [15], the LAIs for crops and tree belts were set to 2.6 and 5.7, respectively; the average leaf inclination angles were set to 57.3° and 26.76°, respectively; and the average canopy heights were 1.6 m and 28.4 m, respectively. In the crop area, the row width was 0.5 m, and the distance between two plants on the same row was 0.25 m. Based on measurements, the fractions of direct solar irradiance were set to 0.876 and 0.923 for the red and NIR bands, respectively. In addition to field measurements, a digital elevation model (DEM) from light detection and ranging (LIDAR) data obtained on June 10, 2012, was also used to determine the position and height information of trees. In this study, individual corn and tree canopies were generated by an extended L-system and OnyxTREE software, respectively [10, 16]. Therefore, the 3D scene corresponding to this study area was generated. It should be noted that because the specific location of corn was unknown, the simulated corn scene based on the row structure and direction did not exactly match the actual scene. Thus, we did not validate the model by using observations of the whole study area and focused on the pixel scale.

IV. Results

A. Intercomparison with a CPU-based model

Fig. 4 (a) and (b) display BRF results for the red and NIR bands, respectively. The simulated red and NIR BRFs by the proposed model agreed well with those simulated by LESS, with their root mean squared errors (RMSEs) lower than 0.001 and 0.003, respectively, and their coefficients of determination (R^2) were both larger than 0.99. As shown in Fig. 4(c), the simulated directional BTs by the proposed model also displayed good agreement with those simulated by LESS, with RMSEs lower than 0.06 K and R^2 larger than 0.99. Nevertheless, relative to LESS, the proposed model produced a slight underestimation in the hotspot area.

Scatter plots of the simulated results for each pixel between two models are given in Fig. 5. The simulated results of the proposed model agreed well with those of LESS. The RMSEs were lower than 0.004, 0.017 and 0.365 K for the red, NIR and BT images, respectively, and the R^2 values were all larger than 0.98. The evaluation results for 1.0 m-resolution images were better than those for 0.2 m-resolution images. The biases in the red and NIR images were lower than 0.001; however, a slight overestimation appeared for BTs with values of 0.052 K and 0.048 K for cases with spatial resolutions of 1.0 m and 0.2 m, respectively.

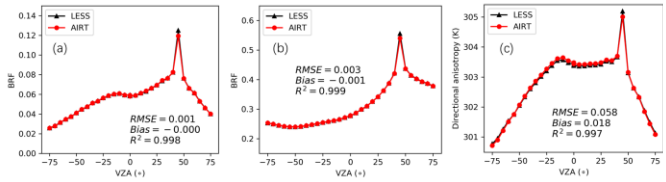

Fig. 4. Comparison of simulated VNIR BRF and LST directional anisotropies between two models. (a), (b) and (c) are the results for the red, NIR and TIR bands, respectively.

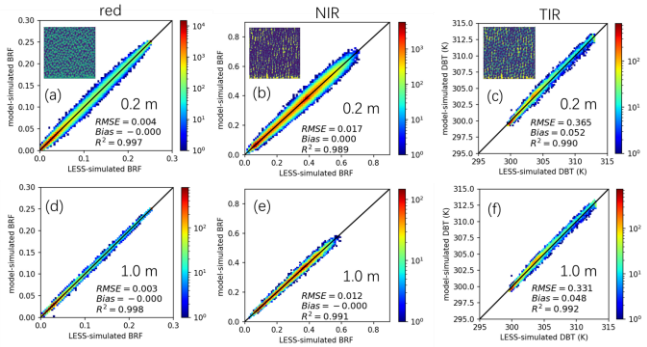

Fig. 5. Scatter plots of simulated results of two models. (a-c) and (d-f) are for spatial resolutions of 0.2 and 1.0 m, respectively.

B. Performance efficiency

Relative to using a CPU solution, a GPU-based solution can simulate by simultaneously using many computer cores. In this study, a simple comparison of the operational efficiency was performed, as shown in Table 1, for two levels of devices. The low-level devices corresponded to entry-level GPU and CPU devices, which are basic configurations used for many design processes and computer games. Although high-level devices perform better than low-level devices, they are all personal application levels carried on the Dell workstation and HP computer, respectively. The low-level and high-level GPU devices were a GeForce RTX 2060 Super and a GeForce RTX 3090, respectively; these devices used 2176 and 10496 NVIDIA Compute Unified Device Architecture (CUDA) cores. An Intel Core i9-9980 HK and a Xeon Silver 4214 were selected as the low-level and high-level CPU devices, respectively. These devices had 8 cores (16 threads) and 24 cores (48 threads) with CPU clock speeds of 2.9 GHz and 2.19 GHz, respectively. Four groups of images were used with 1000×1000 pixels and tree numbers ranging from 50000 to 300000. The calculation time for the GPU-based solution was obviously shorter than that for the CPU-based solution. For these four cases, there was no obvious difference in the calculations performed with the high-level and low-level GPU devices. With an increasing number of trees, the calculation time of the GPU model did not significantly increase. The data preparation/input steps also took some time, approximately 10 seconds, and the destruction of data at the end of simulations also took approximately 5 seconds. According to this comparison, a CPU-based solution could achieve good performance when applied for analysis or validation. However, in an inversion study, many iterations are needed; for a 1000-iteration simulation in an ideal situation, the run time of a CPU-based model is approximately 16-32 hours, whereas that of a GPU-based model can be less than 5.0 minutes. According to this comparison, the GPU-based solution is more suitable for some inversion studies relative to a CPU solution.

Table 1 The performance efficiency of GPU and CPU solutions

		Low-level (s)		High-level (s)	
pixels	trees	CPU-based	GPU-based	CPU-based	GPU-based
1000×1000	50000	81.36	<0.3	55.92	<0.3
1000×1000	100000	101.34	<0.3	77.34	<0.3
1000×1000	200000	163.14	<0.3	105.84	<0.3
1000×1000	300000	203.88	<0.3	109.74	<0.3

C. Validation based on airborne measurements

Figs. 6 (a) and (b) display the measured and simulated BRFs for the selected mixed scene in the red and NIR bands, respectively. Because the VAAs of the observations were almost the same as the SAAs, the hotspot effect can be found. The BRFs in the red and NIR bands reached 0.037 and 0.24, respectively. The simulated BRFs agreed well with the airborne measurements, with RMSEs lower than 0.003 and 0.020 for the red and NIR bands, respectively, and the R^2 were both larger than 0.95. Fig. 6(c) displays a comparison of the DAs of BTs between the simulations and measurements. The TIR DAs were defined by directional BTs minus their mean value. The difference between maximum and minimum DA was larger than 1.7 K. The simulated BT results also exhibit good agreement with those measured by WIDAS, with an RMSE lower than 0.20 K and a R^2 larger than 0.94. Relative to the validation results in the red and NIR bands, the validation results in the TIR band were slightly worse. Notably, in addition to the spectral properties, the thermal properties of components were also required for TIR simulations, which may induce uncertainties.

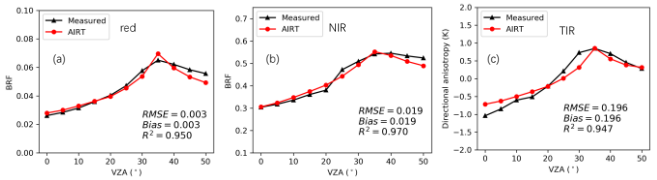

Fig. 6. The comparison between the measured and simulated VNIR BRF and TIR directional anisotropies (DA) of BTs. (a), (b) and (c) are the results for the red, NIR and TIR bands, respectively.

D. Limitations

The proposed GPU-based solution displays good application potential. Nevertheless, some limitations also exist. This GPU-based solution requires state-of-the-art GPU devices. If an old version of a GPU device is used, there may be incompatibilities in device support, or the efficiency of the model may be affected. On the other hand, a CPU-based model would have a wider scope of application because all computers have a CPU but not necessarily a GPU. Although this limit will decrease, it would be good to introduce such a GPU-based solution into an existing CPU-based model for wide and fast performance. It should be mentioned that double coding is not available for some GPU graphic cards. For accurate simulation, a professional computer card is necessary, but the price will be much more expensive. In addition, it is necessary to validate the GPU-based 3D model by using more measurements. Currently, through the use of UAVs, this model could be further validated in the future.

V. Conclusion

With the development of high-resolution satellite and UAV data, radiation and shadow effects from adjacent pixels have become inevitable in inversion and analysis studies. 3D models are vital tools for assessing surface 3D structures in RS studies. In this study, we proposed a GPU-based solution for fast fine-scale RT simulation. An intercomparison between 3D CPU- and GPU-based solutions indicated that with the parallel operation advantage, the efficiency of the proposed GPU-based solution was significantly faster than that of a CPU-based solution. For the same simulation task, the run speed of a GPU-based RT model can be approximately 1/100 of that of CPU-based model. And the simulation accuracy of two solutions is similar. An evaluation based on airborne multiangle measurements also indicated the proposed solution was satisfactory for simulating the red and NIR bidirectional reflectance factor and brightness temperature directional anisotropies, with RMSEs lower than 0.003, 0.019 and 0.20 K, respectively. Considering the simulation accuracy and efficiency, a GPU-based model will play a vital role when studying high-resolution RS data.

VI. References

[1] M. Weiss, F. Jacob, and G. Duveiller, "Remote sensing for agricultural applications: A meta-review," *Remote Sensing of Environment*, vol. 236, p. 111402, 2020/01/01/ 2020, doi: https://doi.org/10.1016/j.rse.2019.111402.

[2] Z. Zhu *et al.*, "Understanding an urbanizing planet: Strategic directions for remote sensing," *Remote Sensing of Environment*, vol. 228, pp. 164-182, 2019/07/01/ 2019, doi: https://doi.org/10.1016/j.rse.2019.04.020.

[3] D. P. Roy *et al.*, "Landsat-8: Science and product vision for terrestrial global change research," *Remote sensing of Environment*, vol. 145, pp. 154-172, 2014.

[4] Y. Yamaguchi, A. B. Kahle, H. Tsu, T. Kawakami, and M. Pniel, "Overview of advanced spaceborne thermal emission and reflection radiometer (ASTER)," *IEEE Transactions on geoscience and remote sensing*, vol. 36, no. 4, pp. 1062-1071, 1998.

[5] S.-B. Duan *et al.*, "Influence of adjacency effect on high-spatial-resolution thermal infrared imagery: Implication for radiative transfer simulation and land surface temperature retrieval," *Remote Sensing of Environment*, vol. 245, p. 111852, 2020.

[6] J.-P. Gastellu-Etchegorry, V. Demarez, V. Pinel, and F. Zagolski, "Modeling radiative transfer in heterogeneous 3-D vegetation canopies," *Remote sensing of environment*, vol. 58, no. 2, pp. 131-156, 1996.

[7] J.-L. Widlowski, T. Lavergne, B. Pinty, M. Verstraete, and N. Gobron, "Rayspread: A virtual laboratory for rapid BRF simulations over 3-D plant canopies," in *Computational methods in transport*: Springer, 2006, pp. 211-231.

[8] H. Huang, W. Qin, and Q. Liu, "RAPID: A Radiosity Applicable to Porous IndiviDual Objects for directional reflectance over complex vegetated scenes," *Remote Sensing of Environment*, vol. 132, pp. 221-237, 2013.

[9] Y. Wang *et al.*, "DART-Lux: An unbiased and rapid Monte Carlo radiative transfer method for simulating remote sensing images," *Remote Sensing of Environment*, vol. 274, p. 112973, 2022/06/01/ 2022, doi: https://doi.org/10.1016/j.rse.2022.112973.

[10] J. Qi *et al.*, "LESS: LargE-Scale remote sensing data and image simulation framework over heterogeneous 3D scenes," *Remote Sensing of Environment*, vol. 221, pp. 695-706, 2019.

[11] J. Jiang, M. Weiss, S. Liu, N. Rochdi, and F. Baret, "Speeding up 3D radiative transfer simulations: A physically based metamodel of canopy reflectance dependency on wavelength, leaf biochemical composition and soil reflectance," *Remote Sensing of Environment*, vol. 237, p. 111614, 2020/02/01/ 2020, doi: https://doi.org/10.1016/j.rse.2019.111614.

[12] C. Jiang and H. Fang, "GSV: a general model for hyperspectral soil reflectance simulation," *International Journal of Applied Earth Observation and Geoinformation*, vol. 83, p. 101932, 2019/11/01/ 2019, doi: https://doi.org/10.1016/j.jag.2019.101932.

[13] N. Vilfan, C. v. d. Tol, O. Muller, U. Rascher, and W. Verhoef, "Fluspect-B: A model for leaf fluorescence, reflectance and transmittance spectra," *remote sensing of environment*, vol. 186, pp. 596-615, 12/1/2016 2016, doi: 10.1016/j.rse.2016.09.017.

[14] Z. Bian *et al.*, "Modeling the Temporal Variability of Thermal Emissions From Row-Planted Scenes Using a Radiosity and Energy Budget Method," *IEEE Transactions on Geoscience and Remote Sensing*, vol. 55, no. 10, pp. 6010-6026, 2017, doi: 10.1109/TGRS.2017.2719098.

[15] Y. Zeng *et al.*, "A radiative transfer model for heterogeneous agro-forestry scenarios," *IEEE Transactions on Geoscience and Remote Sensing*, vol. 54, no. 8, pp. 4613-4628, 2016.

[16] Q. H. Liu, H. G. Huang, W. H. Qin, K. H. Fu, and X. W. Li, "An extended 3-D radiosity-graphics combined model for studying thermal-emission directionality of crop canopy," (in English), *IEEE Transactions on Geoscience & Remote Sensing*, Article vol. 45, no. 9, pp. 2900-2918, Sep 2007, doi: 10.1109/tgrs.2007.902272.

Dear editor:

We hereby submit the manuscript entitled “A GPU-based solution for ray tracing 3D radiative transfer model for optical images”. All authors have read this manuscript and anticipate your consideration for publication in IEEE Geoscience and Remote Sensing Letters as a letter. None of the material related to this manuscript has been published or is under consideration for publication elsewhere, including the internet. We submit this manuscript based on the following reasons:

1. Over the past 20 years there has been a significant increase in high resolution remote sensing images. A three-dimensional (3D) radiative transfer model is usually viewed as a prerequisite when studying high resolution remote sensing data. The 3D radiative transfer modelling is studied in this paper.
2. A fast fine-scale GPU-based 3D model was proposed in this paper by introducing state-of-art computer graphics technology. The computation efficiency of the proposed model is significantly improved, and the simulation accuracy is as good as that of CPU-based model.

We would be very grateful if the submitted manuscript could be reviewed and considered for publication in IEEE Geoscience and Remote Sensing Letters.

Your kind considerations will be greatly appreciated.

With best regards,
Sincerely Yours,
Zunjian BIAN